Spectral identification of electron-nuclear spin defects in diamond

Alexandre Cooper,[1,2] Won Kyu Calvin Sun,[1] Jean-Christophe Jaskula,[1] and Paola Cappellaro[1,*]

[1] *Department of Nuclear Science and Engineering and Research Lab of Electronics, Massachusetts Institute of Technology, Cambridge, MA 02139, USA*

[2] *Department of Physics, Mathematics and Astronomy, California Institute of Technology, Pasadena, CA 91125, USA*

(Dated: July 4, 2018)

Nitrogen-vacancy centers in diamond are sensitive probes of time-varying magnetic fields that can be used to identify unknown spin defects in their nearby environment. Performing spectral quantum measurements on such single quantum probes enables gaining information about the internal structure and dynamics of nearby spin defects that would otherwise be inaccessible through direct or indirect measurements with classical probes. Here, we identify a system composed of two electron-nuclear spin defects in a diamond crystal by performing a series of spectral identification measurements using a single nitrogen-vacancy center in diamond. Besides enabling the identification of new spin defects and studies of their formation mechanisms, these techniques will be useful for scaling up quantum systems by converting environmental spin defects into quantum resources.

Quantum devices that exploit the spins of individual impurity atoms or defect sites in solid-state materials offer promising applications in quantum communication [1–3], quantum information processing [4–6] and quantum sensing [7, 8]. Color centers with robust optical transitions and long-lived spin degrees of freedom are especially attractive to build optically interconnected networks of quantum registers [9–11] and optical transducers of time-varying magnetic fields at the atomic scale [12–14]. The most studied of such color centers is the nitrogen-vacancy (NV) center in diamond, because of its outstanding optical and spin properties under ambient conditions [15].

An important problem with building scalable quantum devices based on synthetic NV centers is the existence of environmental spin defects, predominantly created as byproducts of the NV creation process, such as nitrogen-related centers, vacancies, and their aggregates [16]. Whereas these spin defects usually cause deleterious magnetic field fluctuations responsible for NV decoherence [17], they could rather serve as additional quantum resources were their spin properties known and under control [18, 19]. Although many paramagnetic defects in diamond have been studied using electron spin resonance measurements on large spin ensembles [20], novel quantum applications require characterizing single electron spin defects, which is impossible using standard magnetic induction detection. Spectral identification techniques are therefore needed to characterize the spin properties of single electron-nuclear spin defects coherently coupled to NV centers [21–27], as this would expand the realm of spin defects accessible for practical quantum applications, such as the transfer of quantum information between distant quantum registers [28–30] and the improvement in sensitivity of quantum sensors [19, 31–33].

Here, we demonstrate spectral identification techniques based on double electron-electron resonance (DEER) measurements on a single NV center to characterize the spin properties of two unknown electron-nuclear spin systems in diamond. We exploit the non-trivial transformation of the spin Hamiltonian under rotation of the external magnetic field to estimate the parameters of the unknown spin systems in a manner analogous to tomographic imaging reconstruction.

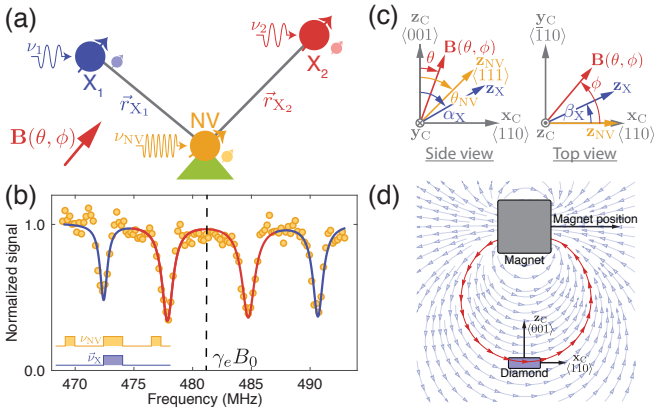

FIG. 1. **Identifying two electron-nuclear spin defects in diamond.** (a) A single nitrogen-vacancy center (NV) interacts with two unknown electron-nuclear spin defects (X_1, X_2) in diamond in the presence of a tunable static magnetic field $\mathbf{B}(\theta, \phi)$. Resonant microwave pulses selectively drive each electron spin, while an optical laser pulse initializes and measures the spin state of the NV electron spin. (b) The spin-echo double-resonance spectrum exhibits two resolved hyperfine doublets centered around the free-electron resonance frequency associated with X_1 (blue, outer spectral lines) and X_2 (red, inner spectral lines). (c) The polar and azimuthal angles that parametrize the orientation of the static magnetic field and the principal axes of the hyperfine tensors are defined with respect to the crystallographic axes of the diamond crystal. (d) The strength and orientation of the static magnetic field is varied by translating a permanent magnet with respect to the diamond sample, whose edge is cut along the $\langle 110 \rangle$ crystallographic axis.

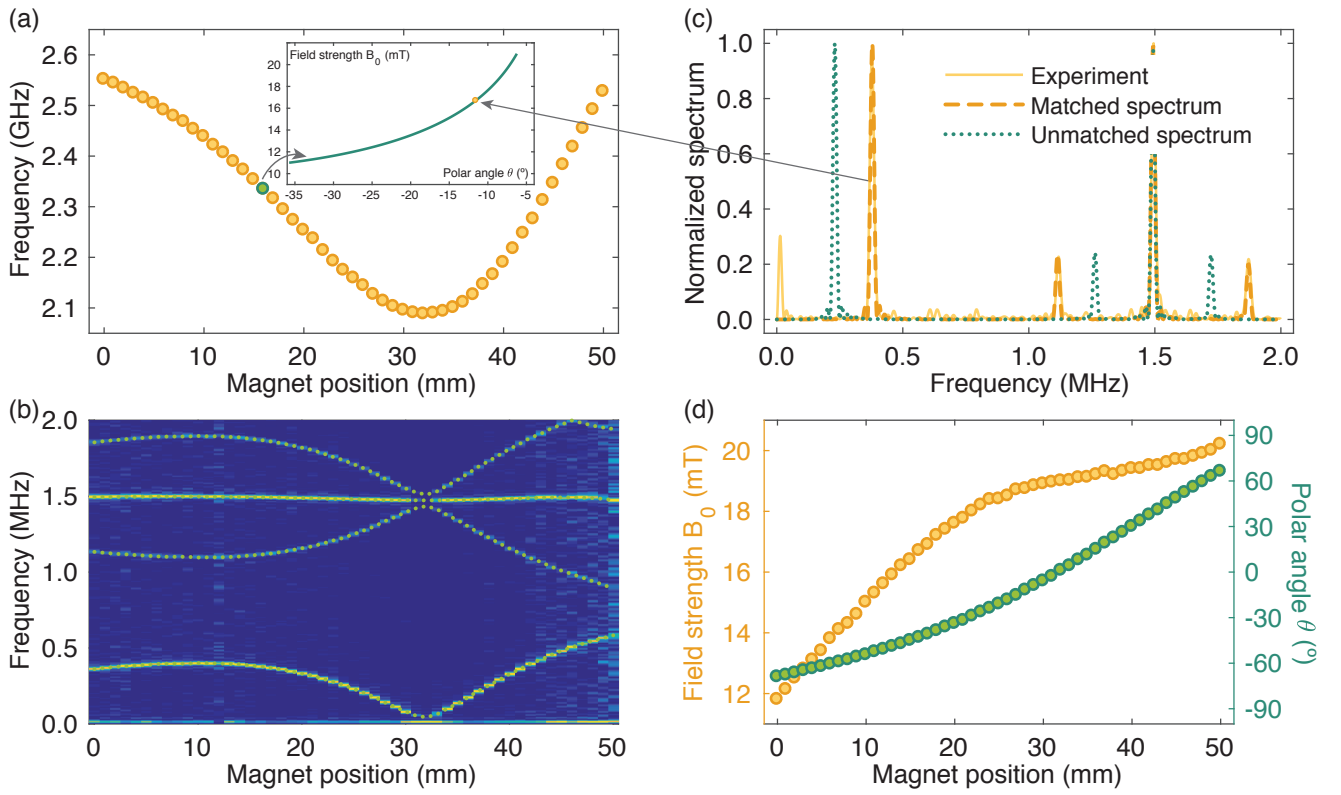

FIG. 2. **Measuring the strength and orientation of the static magnetic field.** (a) Measurements of the resonance frequency of the NV electron spin for various magnet positions. For each magnet position, there exist multiple values of the strength and orientation of the magnetic field that results in the same NV resonance frequency (inset). (b) Measurements of the electron-spin-echo envelope modulation (ESEEM) of the NV electron spin for various magnet positions. The spectral lines at the nuclear frequencies result from hyperfine mixing with the host N-15 nuclear spin in the presence of a non-axial magnetic field. (c) For each magnet position, the field strength and polar angle are unambiguously determined by finding the simulated spectrum that best matches the measured spectrum. (d) Field strength and polar angle of the magnetic field recovered from a series of spectral measurements on the NV electron spin.

Because of the importance of precisely quantifying the strength and orientation of the static magnetic field, we first perform vectorial magnetometry measurements using the NV center. We then perform spectral identification measurements on the two electron-nuclear spin systems to characterize their hyperfine tensor and locate their position in the diamond crystal.

Experimental system—Our experimental system consists of a single NV center interacting through magnetic dipole-dipole interaction with two unknown electron-nuclear spin defects (Fig. 1a), which were randomly created by implanting N-15 nitrogen ions through nanoapertures in an isotopically-enriched C-12 diamond crystal [34]. The electron spin of each defect is coherently manipulated using resonant microwave pulses, while only the NV center is perturbed by the optical excitation pulse needed for spin-state initialization and spin-dependent fluorescence measurements.

We first measured the spin-echo double-resonance (SEDOR) spectrum with a recoupled spin-echo sequence [35], which probes the loss in coherence of the NV electron spin after being selectively recoupled to an electron spin transition coherently driven with a simultaneous π-pulse. We identified four resolved spectral lines centered around the resonance frequency expected for a free electron spin (Fig. 1b), which we attributed to two hyperfine doublets associated with two electron-nuclear spins systems, X_1 and X_2, each modeled by an electronic spin $S = 1/2$ and a nuclear spin $I = 1/2$. The large hyperfine splitting spectrally labels each electron-nuclear spin defect, enabling selective addressability of each hyperfine transition with negligible crosstalk.

The system identification problem consists in estimating the parameters of the spin Hamiltonian describing each of the two electron-nuclear spin systems,

$$\mathcal{H}(\theta,\phi) = \beta_e \, \underline{B} \cdot \underline{\underline{g}} \cdot \underline{S} + \underline{S} \cdot \underline{\underline{A}} \cdot \underline{I} - g_n \beta_n \, \underline{B} \cdot \underline{I}, \quad (1)$$

where $\underline{B} = \underline{B}(\theta,\phi)$ is the static magnetic field vector of norm B_0, $\underline{\underline{g}}$ is the g tensor of the electron spin, $\underline{\underline{A}}$ is the hyperfine interaction tensor, g_n is the g factor of the nuclear spin, β_e is the Bohr magneton, and β_n is the nuclear magneton (we set $\hbar = 1$). The general approach to

perform spectral identification is to measure the energy eigenvalues of $\mathcal{H}(\theta,\phi)$ by varying the orientation of the static magnetic field $\underline{B}(\theta,\phi)$, which is parametrized by the polar and azimuthal angles, θ and ϕ, defined with respect to the crystallographic axes of the diamond crystal (Fig. 1c).

Characterizing the strength and orientation of the static magnetic field—To systematically vary the orientation of the static magnetic field at the location of the NV center, we mounted a 25.4 mm-edge cubic magnet on a linearly-actuated translation stage with rotational degrees of freedom (Fig. 1d). We aligned the magnetization axis of the magnet along the $\langle 110\rangle$ crystallographic axis of the diamond crystal in such a way that displacing the magnet along its magnetization axis rotated the magnetic field by the polar angle θ in the $\langle 001\rangle \times \langle 110\rangle$ ($\phi = 0°$) crystallographic plane. This was confirmed by performing spectral measurements on an ensemble of NV centers and observing the spectral overlap of the resonance frequencies of two out of the four NV crystallographic classes. Fixing the position of the magnet at the polar angle $\theta = 90°$ and rotating the magnet along its vertical axis further rotated the azimuthal angle ϕ of the magnetic field in the $\langle 110\rangle \times \langle \bar{1}10\rangle$ crystallographic plane.

To quantify the strength and orientation of the static magnetic field at each position of the magnet, we first measured the resonance frequency of the NV electron spin in the $m_s \in \{0,-1\}$ manifold using a continuous wave electron spin resonance (cw-esr) sequence (Fig. 2a). The set of measured frequencies was, however, not sufficient to uniquely determine the strength and orientation of the static magnetic field; there indeed existed an infinite number of admissible values for (B_0,θ) that resulted in the same resonance frequency (Fig. 2b).

To resolve this ambiguity, we further measured the frequencies of the electron spin-echo envelope modulation (ESEEM) [36] caused by the strong dipolar coupling to the intrinsic N-15 nuclear spin of the NV center (Fig. 2c). In the presence of a static magnetic field oriented along a direction different from the molecular axis of the NV center ($\langle 111\rangle$ crystallographic axis), the bare energy levels of the NV electron spin and N-15 nuclear spin are mixed, such that the spin-echo signal is modulated at the nuclear frequencies and their combinations, $\{\nu_1, \nu_0, \nu_1 \pm \nu_0\}$. These frequencies correspond to the quantization energies of the nuclear spin conditional on the NV electron spin being in the $m_s = 0$ or $m_s = -1$ spin states.

We numerically simulated the ESEEM spectrum [37] by diagonalizing the electron-nuclear spin Hamiltonian of the NV center for different values of the strength and orientation of the static magnetic field. For each position of the magnet, we searched for the field parameters (B_0,θ) that best reproduced the measured ESEEM spectrum (Fig. 2b) under the constraint of a known NV resonance frequency. Following this approach, we determined a unique pair of admissible values for the field parameters at each magnet position (Fig. 2d).

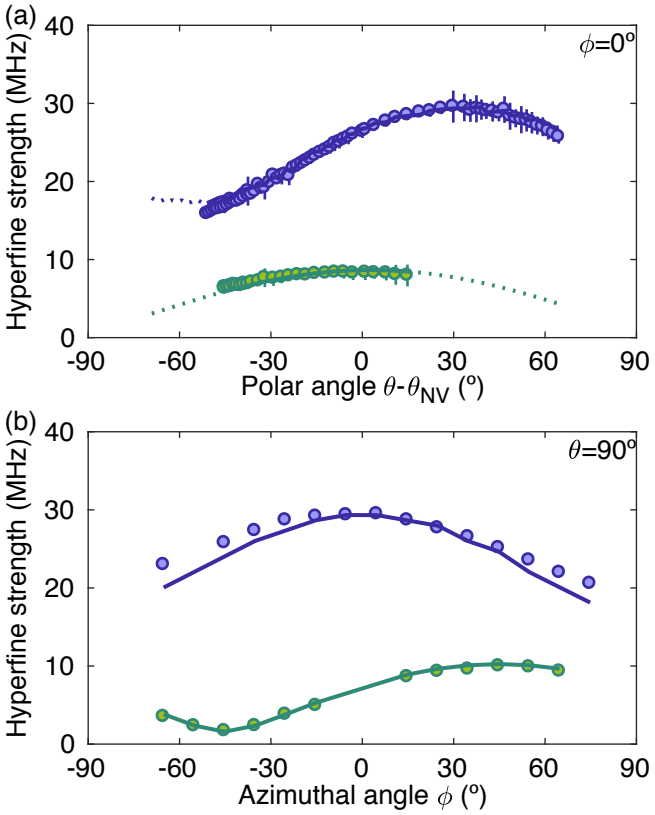

FIG. 3. **Characterizing the hyperfine tensors of two electron-nuclear spin defects.** (a) Measurements of the hyperfine strength for various polar angles θ of the magnetic field in the azimuthal plane $\phi = 0$. (b) Measurements of the hyperfine strength for various azimuthal angles ϕ of the magnetic field in the polar plane $\theta = 90°$. The solid line is the best least-square fit of both sets of experimental data to the eigenvalues of an axially-symmetric hyperfine tensor with four free parameters.

Characterizing the hyperfine tensors—After establishing a reliable mapping between the position of the magnet and the strength and orientation of the static magnetic field, we set forth to characterize the hyperfine tensors of the two unknown electron-nuclear spin defects following an approach akin to tomographic imaging reconstruction.

From a geometric point of view, the hyperfine tensor can indeed be represented as an ellipsoid, whose dimensions are given by the principal components of the hyperfine tensor, $\{A_x, A_y, A_z\}$, and whose orientation is given by the principal angles of the hyperfine tensor, $\{\alpha,\beta,\gamma\}$. Rotating the magnetic field around a fixed axis generates multiple tomographic cuts of the hyperfine ellipsoid that allow estimating the ellipsoid parameters.

We estimated the hyperfine parameters by monitoring the change in the frequency splitting of the two hyperfine doublets as a function of the orientation of the static magnetic field (Fig. 3). To simplify the spectral identification problem, we assumed the hyperfine tensor

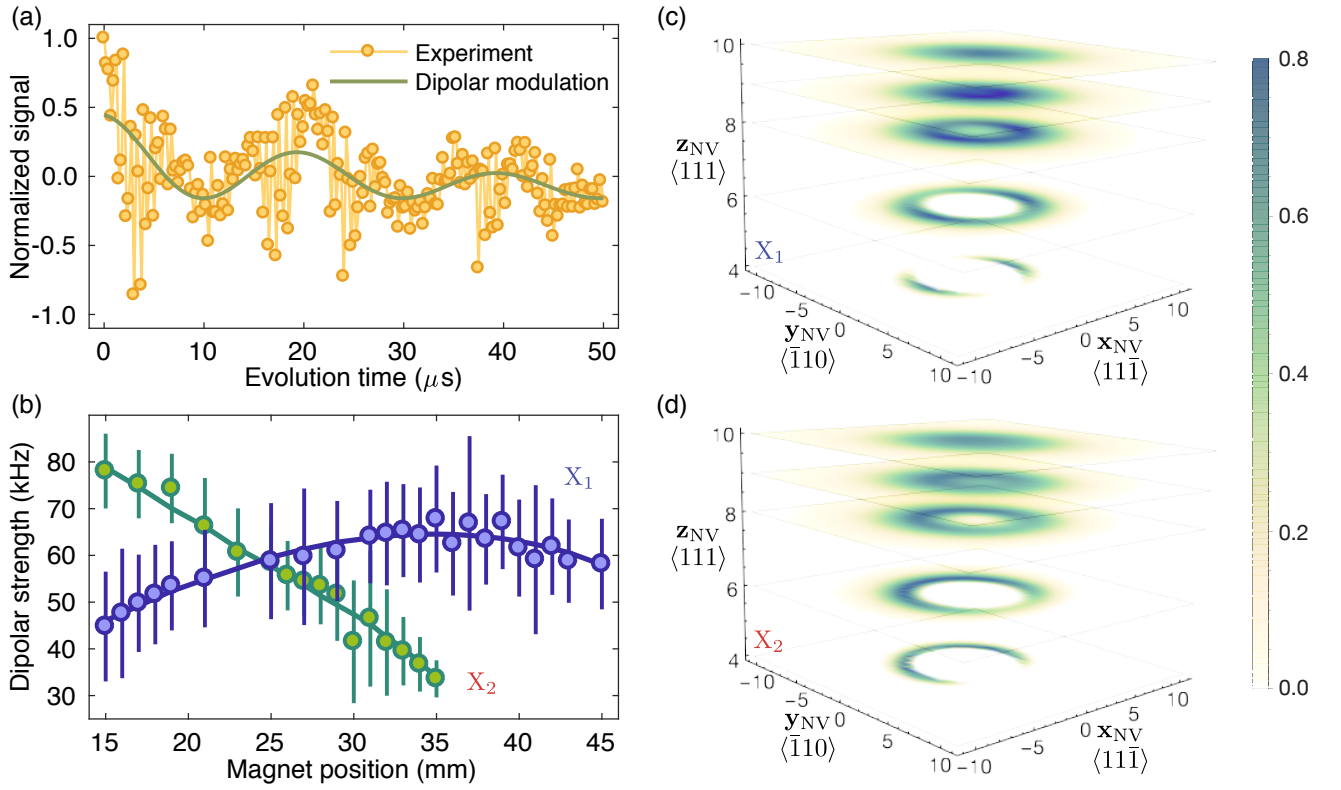

FIG. 4. **Locating two electron-nuclear spin defects in the diamond crystal.** (a) Example measurements of the dipolar coupling strength using a recoupled spin-echo sequence in the presence of a non-axial magnetic field. The slow modulation (solid line) is caused by the dipolar interaction with the X electron spin defect, whereas the fast modulation is caused by the hyperfine mixing with the host N-15 nuclear spin. (b) Measurements of the dipolar coupling strength to X_1 (blue) and X_2 (green) for various magnet positions. The solid line is the best least-square fit to the eigenvalues of the interacting spin Hamiltonian with three free parameters parametrizing the location of the unknown spin defect. (c-d) Probability distribution maps of the location of the unknown spin defects X_1 (top) and X_2 (bottom) defined with respect to the coordinate frame of the NV center placed at the origin. The darker color indicates a higher probability of finding the unknown spin defect at this specific location.

$\underline{\underline{A}}$ to be axially symmetric (i.e., $A_x = A_y \equiv A_\perp$), neglected the nuclear Zeeman term, and chose the g tensor to be isotropic with its principal value equal to the electron spin g-factor (i.e., $\underline{\underline{g}} = g_e \cdot \underline{\underline{1}}$). These assumptions were consistent with our set of experimental measurements, which could be further extended to reliably distinguish between an axially-symmetric tensor and a full tensor [34]. Characterizing the unknown electron-nuclear spin defects thus involved measuring a set of four unknown parameters, $\{A_\perp, A_\parallel, \alpha_X, \beta_X\}$ (Fig. 1c).

We simultaneously fitted the set of all measured hyperfine strength values to the set of eigenvalues obtained by diagonalizing the spin Hamiltonian of Eq. (1). We obtained $A_\perp = 17.2(3)$, $A_\parallel = 29.4(2)$, $\alpha_X = 0(2)$, $\beta_X = 87(2)$ for the first spin defect (X_1) and $A_\perp = 1.6(3)$, $A_\parallel = 11.2(2)$, $\alpha_X = 45(2)$, $\beta_X = 66(2)$ for the second spin defect (X_2). We searched the scientific literature [20, 38–43] for paramagnetic defects sharing these parameters, but could not find any suitable candidates, possibly indicating that we were dealing with previously unstudied spin defects in diamond. We believe these defects to be nitrogen-related defects created during nitrogen ion implantation or silicon-related centers resulting from the use of a silicon implantation mask. Although additional spectral measurements will be required to uniquely identify these two spin defects, as of interest to materials science, the measured hyperfine parameters provide a consistent description of our spin system that is sufficient to control and exploit its spin degrees of freedom for practical quantum applications.

Characterizing the magnetic dipolar interaction tensors—To spatially locate the unknown spin defects in the environment of the NV center, we measured the change in the dipolar interaction strength as we rotated the polar angle θ of the static magnetic field in the azimuthal plane $\phi = 0$. Because the NV and X electron spins are quantized along different axes, the transformation of the dipolar interaction tensor under rotation of the magnetic field is non-trivial [34]. Another complication is that, as the magnetic field is rotated away from the NV molecular

axis, the NV coherence signal becomes modulated by the hyperfine interaction with the intrinsic N-15 nuclear spin, in addition to the desired modulation due to the dipolar interaction with the recoupled X electron spin (Fig. 4a).

We first measured the dipolar coupling strength between the NV electron spin and each X electron spins by extracting the low-frequency dipolar contribution to the modulation of the SEDOR signal (Fig. 4b). We then calculated the dipolar coupling strength for various locations of the spin defects. We finally computed the least square error between the measured values and the calculated values to generate probability distribution maps of the location of the two X spin defects with respect to the NV center (Fig. 4c-d). The estimated distance from the NV center at the most probable location is $r_1 = 9.23(3)$ nm and $r_2 = 6.58(3)$ nm for X_1 and X_2 respectively. We further searched for signatures of direct magnetic dipole-dipole interaction between X_1 and X_2, but could not resolve any coherent interaction, indicating that the defects are farther apart to each other than to the NV.

Conclusions—We have demonstrated spectral identification techniques to characterize and locate two unknown electron-nuclear spin defects in the environment of a single NV center in diamond. These techniques are readily applicable to study the physical properties of single paramagnetic defects in diamond or similar host materials such as silicon carbide.

Studying the physical properties of paramagnetic centers created by ion implantation and annealing could guide fabrication techniques, leading to novel approaches to mitigate lattice damage or to create single spin defects with improved coherence and spectral properties. In addition, as spin defects affect the optical, charge, and spin properties of NV centers, characterizing their spin properties enables developing coherent control techniques to effectively suppress their detrimental influence, e.g., by polarizing their spin state or photo-ionizing weakly bounded electrons, or exploit them for practical applications. Finally, as spin defects are representative of molecular structures, e.g., labeled proteins, these techniques can be applied to identify spin systems of greater complexity, including unknown molecular structures placed near the surface of diamond [31, 32]. Future work will focus on converting these hybrid electron-nuclear spin systems into quantum resources for quantum sensing and information processing.

This work was in part supported by NSF grants PHY1415345 and EECS1702716. A. C. also acknowledges financial support by the Fulbright Program and the Natural Sciences and Engineering Research Council of Canada. We are grateful to Chinmay Belthangady and Huiliang Zhang for their experimental support.

* pcappell@mit.edu

[1] L. Childress and R. Hanson, *MRS Bulletin*, **38**, 134 (2013).
[2] W. B. Gao, A. Imamoglu, H. Bernien, and R. Hanson, Nature Photonics **9**, 363 EP (2015).
[3] M. Atatüre, D. Englund, N. Vamivakas, S.-Y. Lee, and J. Wrachtrup, Nature Reviews Materials **3**, 38 (2018).
[4] J. J. L. Morton and B. W. Lovett, *Annual Review of Condensed Matter Physics*, Annual Review of Condensed Matter Physics **2**, 189 (2011).
[5] D. D. Awschalom, L. C. Bassett, A. S. Dzurak, E. L. Hu, and J. R. Petta, Science **339**, 1174 (2013).
[6] T. F. Watson, B. Weber, Y.-L. Hsueh, L. C. L. Hollenberg, R. Rahman, and M. Y. Simmons, Science Advances **3** (2017).
[7] C. L. Degen, F. Reinhard, and P. Cappellaro, Rev. Mod. Phys. **89**, 035002 (2017).
[8] F. Casola, T. van der Sar, and A. Yacoby, Nature Reviews Materials **3**, 17088 EP (2018).
[9] H. J. Kimble, Nature **453**, 1023 EP (2008).
[10] H. Bernien, B. Hensen, W. Pfaff, G. Koolstra, M. S. Blok, L. Robledo, T. H. Taminiau, M. Markham, D. J. Twitchen, L. Childress, and R. Hanson, Nature **497**, 86 EP (2013).
[11] P. C. Humphreys, N. Kalb, J. P. J. Morits, R. N. Schouten, R. F. L. Vermeulen, D. J. Twitchen, M. Markham, and R. Hanson, Nature **558**, 268 (2018).
[12] J. M. Taylor, P. Cappellaro, L. Childress, L. Jiang, D. Budker, P. R. Hemmer, A. Yacoby, R. Walsworth, and M. D. Lukin, Nature Physics **4**, 810 EP (2008).
[13] A. Cooper, E. Magesan, H. N. Yum, and P. Cappellaro, Nature Communications **5**, 3141 EP (2014).
[14] A. Ajoy, U. Bissbort, M. D. Lukin, R. L. Walsworth, and P. Cappellaro, Physical Review X **5**, 011001 (2015).
[15] M. W. Doherty, N. B. Manson, P. Delaney, F. Jelezko, J. Wrachtrup, and L. C. L. Hollenberg, *The nitrogen-vacancy colour centre in diamond*, Physics Reports **528**, 1 (2013).
[16] P. Deák, B. Aradi, M. Kaviani, T. Frauenheim, and A. Gali, Physical Review B **89**, 075203 (2014).
[17] G. de Lange, Z. H. Wang, D. Ristè, V. V. Dobrovitski, and R. Hanson, Science **330**, 60 (2010).
[18] L. Schlipf, T. Oeckinghaus, K. Xu, D. B. R. Dasari, A. Zappe, F. F. de Oliveira, B. Kern, M. Azarkh, M. Drescher, M. Ternes, K. Kern, J. Wrachtrup, and A. Finkler, Science Advances **3** (2017), 10.1126/sciadv.1701116.
[19] G. Goldstein, P. Cappellaro, J. R. Maze, J. S. Hodges, L. Jiang, A. S. Sørensen, and M. D. Lukin, Physical Review Letters **106**, 140502 (2011).
[20] J. H. N. Loubser and J. A. van Wyk, Reports on Progress in Physics **41**, 1201 (1978).
[21] R. J. Epstein, F. M. Mendoza, Y. K. Kato, and D. D. Awschalom, Nature Physics **1**, 94 EP (2005).
[22] R. Hanson, F. M. Mendoza, R. J. Epstein, and D. D. Awschalom, Physical Review Letters **97**, 087601 (2006).
[23] F. Shi, Q. Zhang, B. Naydenov, F. Jelezko, J. Du, F. Reinhard, and J. Wrachtrup, Phys. Rev. B **87**, 195414 (2013).
[24] A. O. Sushkov, I. Lovchinsky, N. Chisholm, R. L. Walsworth, H. Park, and M. D. Lukin, Phys. Rev. Lett.

113, 197601 (2014).
[25] M. S. Grinolds, M. Warner, K. De Greve, Y. Dovzhenko, L. Thiel, R. L. Walsworth, S. Hong, P. Maletinsky, and A. Yacoby, Nature Nanotechnology **9**, 279 EP (2014).
[26] H. S. Knowles, D. M. Kara, and M. Atatüre, Phys. Rev. Lett. **117**, 100802 (2016).
[27] E. L. Rosenfeld, L. M. Pham, M. D. Lukin, and R. L. Walsworth, Physical Review Letters **120**, 243604 (2018).
[28] P. Neumann, R. Kolesov, B. Naydenov, J. Beck, F. Rempp, M. Steiner, V. Jacques, G. Balasubramanian, M. L. Markham, D. J. Twitchen, S. Pezzagna, J. Meijer, J. Twamley, F. Jelezko, and J. Wrachtrup, Nature Physics **6**, 249 EP (2010).
[29] P. Cappellaro, L. Viola, and C. Ramanathan, Physical Review A **83**, 032304 (2011).
[30] N. Y. Yao, L. Jiang, A. V. Gorshkov, Z. X. Gong, A. Zhai, L. M. Duan, and M. D. Lukin, Physical Review Letters **106**, 040505 (2011).
[31] F. Shi, Q. Zhang, P. Wang, H. Sun, J. Wang, X. Rong, M. Chen, C. Ju, F. Reinhard, H. Chen, J. Wrachtrup, J. Wang, and J. Du, Science **347**, 1135 (2015).
[32] I. Lovchinsky, A. O. Sushkov, E. Urbach, N. P. de Leon, S. Choi, K. De Greve, R. Evans, R. Gertner, E. Bersin, C. Müller, L. McGuinness, F. Jelezko, R. L. Walsworth, H. Park, and M. D. Lukin, Science **351**, 836 (2016).
[33] D. A. Simpson, R. G. Ryan, L. T. Hall, E. Panchenko, S. C. Drew, S. Petrou, P. S. Donnelly, P. Mulvaney, and L. C. L. Hollenberg, Nature Communications **8**, 458 (2017).
[34] See Supplemental Material for details of the experiment and theoretical models.
[35] G. de Lange, T. van der Sar, M. Blok, Z.-H. Wang, V. Dobrovitski, and R. Hanson, Scientific Reports **2**, 382 EP (2012).
[36] W. B. Mims, Phys. Rev. B **5**, 2409 (1972).
[37] S. Stoll and A. Schweiger, Journal of Magnetic Resonance **178**, 42 (2006).
[38] J. Isoya, H. Kanda, Y. Uchida, S. C. Lawson, S. Yamasaki, H. Itoh, and Y. Morita, Physical Review B **45**, 1436 (1992).
[39] J. A. van Wyk, O. D. Tucker, M. E. Newton, J. M. Baker, G. S. Woods, and P. Spear, Physical Review B **52**, 12657 (1995).
[40] S. Felton, B. L. Cann, A. M. Edmonds, S. Liggins, R. J. Cruddace, M. E. Newton, D. Fisher, and J. M. Baker, Journal of Physics: Condensed Matter **21**, 364212 (2009).
[41] S. Liggins, M. E. Newton, J. P. Goss, P. R. Briddon, and D. Fisher, Physical Review B **81**, 085214 (2010).
[42] M. K. Atumi, J. P. Goss, P. R. Briddon, F. E. Shrif, and M. J. Rayson, Journal of Physics: Condensed Matter **25**, 065802 (2013).
[43] B. L. Green, M. W. Dale, M. E. Newton, and D. Fisher, Physical Review B **92**, 165204 (2015).

SUPPLEMENTAL MATERIAL

Experimental system

The nitrogen-vacancy (NV) center in diamond is a point-defect formed by a substitutional nitrogen atom located nearby a vacancy in the diamond lattice. The NV center in its negatively charged state (NV^-) has two unpaired electrons that form a spin-triplet ground state with three magnetic sub-levels, $m_s = \{0, \pm 1\}$ and a zero-field splitting of $\Delta = 2\pi \cdot 2870$ MHz. The NV center has a spin-triplet excited state with a phonon-broaden spin-preserving optical transition in the visible range centered at 637 nm. This optical transition enables spin-state initialization in the $m_s = 0$ ground state by optical pumping and spin-state readout by fluorescence imaging. The host nuclear spin ($I = 1$ for N-14, $I = 1/2$ for N-15), coupled by an anisotropic hyperfine interaction, provides additional degrees of freedom for storing quantum information and assisting in magnetic sensing applications.

We fabricated two-dimensional arrays of confined ensembles of spin defects in a synthetic diamond crystal by implanting N-15 nitrogen ions through circular apertures with a diameter of 30 nm. The diamond substrate was a single crystal chemical vapor deposition (CVD) diamond from Element Six with a 100 μm-thick layer of isotopically enriched 99.999 % C–12 grown on top of a 300 μm-thick electron grade single crystal diamond substrate. The diamond sample was cut with its edge directed along the $\langle 110 \rangle$ crystallographic axis, such that the $\langle 111 \rangle$ molecular axis of the NV center lied in the $\langle 110 \rangle \times \langle 001 \rangle$ crystallographic plane with its transverse projection oriented towards the $\langle 110 \rangle$ edge of the diamond sample. We patterned circular apertures in a 150 nm-thick layer of Poly(methyl methacrylate) (PMMA) using electron-beam lithography with an exposure dose of 1400 $\mu C/cm^2$. We then implanted N-15 nitrogen ions with an energy of 14 keV and a dose of 1e13 cm^{-2}. We chose these implantation energy and dose parameters as a trade-off between increasing the mean distance to the diamond surface and reducing the longitudinal straggling of the nitrogen ions. We further annealed the diamond sample at a temperature of 800 °C for 4 h to promote the mobility of vacancies and create NV centers with a conversion efficiency of less than a few percent. We finally cleaned the surface of the diamond with a boiling mixture of concentrated acids (1:1:1 $H_2SO_4 : HNO_3 : HClO_4$). We routinely cleaned the diamond surface with a piranha acid solution (3:1 $H_2O_2 : H_2SO_4$) and did not observe any modifications of the properties of our spin system.

Numerical simulations with the SRIM software indicated that the spatial distribution of substitutional nitrogen defects in each implanted region was normally distributed with a mean implantation depth of 19.9 nm and a longitudinal straggling of 6.6 nm, greater than the interaction range with surface spins. We searched over more than 150 implanted regions to identify three single NV centers, one of which exhibited a strongly modulated interferometric signal and was thus used in this study. For this NV center, we could not resolve a coherent signal from ensembles of nuclear spins associated with impurities on the surface of the diamond sample or protons of the confocal oil, suggesting a relatively deep NV center.

Characterizing the hyperfine interaction strength

We derive an analytical expression for the hyperfine coupling strength in the secular approximation as a function of the orientation of the static magnetic field. The Zeeman Hamiltonian for the electron spin is given by

$$\begin{aligned} \mathcal{H}_e(\theta, \phi) &= \beta_e \, \underline{B} \cdot \underline{\underline{g}} \cdot \underline{S} && (2) \\ &= g_e \beta_e \, \underline{B} \cdot \underline{S} && (3) \\ &= \omega_e(\cos(\theta) S_z + \sin(\theta)(\cos(\phi) S_x + \sin(\phi) S_y)), && (4) \end{aligned}$$

where $\omega_e = g_e \beta_e B_0$ is the Zeeman energy of the electron spin and

$$\underline{B}(\theta, \phi) = B_0(\sin(\theta)\cos(\phi), \sin(\theta)\sin(\phi), \cos(\theta)), \quad (5)$$

is the magnetic field vector expressed in the crystal frame using the polar and azimuthal angles (θ, ϕ).

The strength of the magnetic field is chosen such that the hyperfine coupling strength is smaller than the electron

spin Zeeman energy, but larger than the nuclear spin Zeeman energy, i.e., $\omega_n \ll \|A\| \ll \omega_e$. Under this assumption, the electron spin is quantized by the Zeeman energy, whereas the nuclear spin is not.

Recall that the hyperfine tensor is fully characterized by its principal components $\{A_x, A_y, A_z\}$, and its orientation with respect to the crystal frame, given by the Euler angles, $\{\alpha, \beta, \gamma\}$. The hyperfine tensor in its principal coordinate frame is thus represented by a diagonal matrix

$$A = \mathrm{diag}[A_x, A_y, A_z], \tag{6}$$

which can be rotated into the crystal frame as

$$\hat{\hat{A}} = R^T \cdot A \cdot R, \tag{7}$$

where R is the rotation matrix describing the transformation of the hyperfine matrix from its principal coordinate frame to the crystal frame,

$$R = \begin{pmatrix} \cos(\gamma)\cos(\beta)\cos(\alpha) - \sin(\gamma)\sin(\alpha) & \cos(\gamma)\cos(\beta)\sin(\alpha) + \sin(\gamma)\cos(\alpha) & -\cos(\gamma)\sin(\beta) \\ -\sin(\gamma)\cos(\beta)\cos(\alpha) - \cos(\gamma)\sin(\alpha) & -\sin(\gamma)\cos(\beta)\sin(\alpha) + \cos(\gamma)\cos(\alpha) & \sin(\gamma)\sin(\beta) \\ \sin(\beta)\cos(\alpha) & \sin(\beta)\sin(\alpha) & \cos(\beta) \end{pmatrix}.$$

For simplicity, assume the magnetic field to be aligned along the z-axis of the crystal frame, such $\underline{B} = B_0 \cdot (0, 0, 1)$ for $\theta = 0$ and $\phi = 0$. The secular hyperfine Hamiltonian is given by

$$\mathcal{H}_h = \vec{S} \cdot \hat{\hat{A}} \cdot \vec{I} \tag{8}$$

$$\approx S_z \hat{A}_z \cdot \vec{I} = S_z(A_{zx} I_x + A_{zy} I_y + A_{zz} I_z), \tag{9}$$

giving rise to an effective hyperfine frequency shift of $C_z = \sqrt{A_{zx}^2 + A_{zy}^2 + A_{zz}^2}$.

In general, the hyperfine coupling strength is given by

$$C_z = \sqrt{\mathrm{Tr}\{(H_e \otimes I_x)H_h\}^2 + \mathrm{Tr}\{(H_e \otimes I_y)H_h\}^2 + \mathrm{Tr}\{(H_e \otimes I_z)H_h\}^2}/4\omega_e. \tag{10}$$

In the case of an isotropic hyperfine tensor, we have

$$C_z^{\mathrm{iso}} = A_z, \tag{11}$$

whereas in the case of an axially symmetric tensor, we have

$$\begin{aligned} C_z^{\mathrm{ax}} \; &= \tfrac{1}{2\sqrt{2}} \big[5A_x^2 + 3A_z^2 - (A_x - A_z)(A_x + A_z) \times \\ &\big(4\cos(2(\alpha-\phi))\sin^2(\beta)\sin^2(\theta) + 4\cos(\alpha-\phi)\sin(2\beta)\sin(2\theta) + \cos(2\beta)(3\cos(2\theta)+1) + \cos(2\theta)\big)\big]^{1/2}. \end{aligned}$$

In the general case of an arbitrary tensor, we can also recover an explicit expression, which is given by

$$\begin{aligned} C_z^2 = [&s(\beta)\left((A_x - A_y)s(\gamma)c(\gamma)s(\theta)s(\alpha-\phi) + A_x s(\beta)c^2(\gamma)c(\theta) + A_y s(\beta)s^2(\gamma)c(\theta)\right) \\ &-\tfrac{1}{4}s(2\beta)s(\theta)c(\alpha-\phi)((A_x - A_y)c(2\gamma) + A_x + A_y - 2A_z) + A_z c^2(\beta)c(\theta)]^2 \\ &+[\tfrac{1}{2}s(\alpha)c^2(\beta)s(\theta)c(\alpha-\phi)((A_x - A_y)c(2\gamma) + A_x + A_y) + c^2(\alpha)s(\theta)s(\phi)\left(A_x s^2(\gamma) + A_y c^2(\gamma)\right) \\ &-c(\alpha)\left((A_x - A_y)s(\beta)s(\gamma)c(\gamma)c(\theta) + s(\alpha)s(\theta)c(\phi)\left(A_x s^2(\gamma) - A_z s^2(\beta)\right) + A_y s(\alpha)c^2(\gamma)s(\theta)c(\phi)\right) \\ &+c(\beta)\left(\tfrac{1}{2}(A_x - A_y)s(2\gamma)s(\theta)c(2\alpha-\phi) + s(\alpha)s(\beta)c(\theta)\left(-A_x c^2(\gamma) - A_y s^2(\gamma) + A_z\right)\right) + A_z s^2(\alpha)s^2(\beta)s(\theta)s(\phi)]^2 \\ &+[s(\alpha)\left(A_x s(\alpha)s^2(\gamma)s(\theta)c(\phi) + (A_x - A_y)s(\gamma)c(\gamma)(s(\beta)c(\theta) - s(\alpha)c(\beta)s(\theta)s(\phi)) + A_y s(\alpha)c^2(\gamma)s(\theta)c(\phi)\right) \\ &+c^2(\alpha)s(\theta)\left(c^2(\beta)c(\phi)\left(A_x c^2(\gamma) + A_y s^2(\gamma)\right) + (A_x - A_y)c(\beta)s(\gamma)c(\gamma)s(\phi) + A_z s^2(\beta)c(\phi)\right) \\ &+c(\alpha)(s(\alpha)c^2(\beta)s(\theta)s(\phi)\left(A_x c^2(\gamma) + A_y s^2(\gamma)\right) + c(\beta)\left(s(\alpha)(A_y - A_x)s(2\gamma)s(\theta)c(\phi) + s(\beta)c(\theta)\left(-A_x c^2(\gamma) - A_y s^2(\gamma) + A_z\right)\right) \\ &-s(\alpha)s(\theta)s(\phi)\left(A_x s^2(\gamma) + A_y c^2(\gamma) - A_z s^2(\beta)\right))]^2. \end{aligned}$$

We fit the data collected as described in the main text to these formulas, where the magnetic field angles θ and ϕ were varied by the magnet translation. We found that the model of an axially symmetric tensor fitted slightly better the data (lower χ^2). Further data points (at different combinations of θ and ϕ) could better discriminate between models.

Characterizing the dipolar interaction strength

In the absence of a static magnetic field, the NV center is quantized along its $\langle 111 \rangle$ molecular axis defined by the strong crystal field responsible for the zero-field splitting $\Delta = 2\pi \cdot 2870$ MHz. In the presence of a weak static magnetic field of strength $\gamma_e B_0 \ll \Delta$, the NV electronic spin is weakly tilted away from its molecular axis, whereas the X electronic spin is predominantly quantized along the external field. This behavior is responsible for a non-trivial transformation of the dipolar interaction tensor under rotation and thus a dependence of the effective dipolar strength as a function of the strength and orientation of the static magnetic field, hence containing information about the spatial location of the X spins with respect to the NV center.

The total spin Hamiltonian describing the interaction between the NV center ($S_{\mathrm{NV}} = 1$, $I_{\mathrm{NV}} = 1/2$) and the X paramagnetic center ($S_{\mathrm{NV}} = 1/2$, $I_{\mathrm{NV}} = 1/2$) is given by

$$\mathcal{H} = \mathcal{H}_{\mathrm{NV}} + \mathcal{H}_{\mathrm{X}} + \mathcal{H}_{\mathrm{NV-X}}, \tag{12}$$

where $\mathcal{H}_{\mathrm{NV}}$ ($\mathcal{H}_{\mathrm{X}}$) is the spin Hamiltonian of the NV center (X spin defect) and $\mathcal{H}_{\mathrm{NV-X}}$ the interaction Hamiltonian describing the magnetic dipolar interaction between the NV electron spin and X electron spin. The dipolar Hamiltonian in its general form is given by

$$\mathcal{H}_{\mathrm{NV-X}} = -\frac{\mu_0}{4\pi}\frac{\gamma_{\mathrm{NV}}\gamma_{\mathrm{X}}\hbar^2}{r^3}(3(\underline{S}_{\mathrm{NV}} \cdot \underline{r})(\underline{S}_{\mathrm{X}} \cdot \underline{r}) - (\underline{S}_{\mathrm{NV}} \cdot \underline{S}_{\mathrm{X}})), \tag{13}$$

where $\underline{r} = (\sin(\alpha)\cos(\gamma), \sin(\alpha)\sin(\gamma), \cos(\alpha))$ is the interatomic vector of norm 1 that join the NV center and X spin defect, parameterized by the distance r between the two centers and the polar and azimuthal angles (α, γ) defined with respect to the NV molecular axis.

Since we can consider the dipolar coupling as a perturbation of each spin Hamiltonian, the only visible component in experiments is the energy-conserving one. Thus, the effective (secular) dipolar coupling strength between the NV electron spin and X electron spin is obtained by computing the eigenvalues of the total dipolar Hamiltonian in the doubly-tilted frame

$$\tilde{\mathcal{H}} = U_{\mathrm{X}}^{-1} U_{\mathrm{NV}}^{-1} \mathcal{H}_{\mathrm{NV-X}} U_{\mathrm{NV}} U_{\mathrm{X}} \tag{14}$$

where U_{NV} (U_{X}) is the unitary transformation diagonalizing $\mathcal{H}_{\mathrm{NV}}$ ($\mathcal{H}_{\mathrm{X}}$).

By projecting the NV electron spin onto an effective two-level system, it is possible to analytically evaluate the secular dipolar strength. In this approximation, valid when the $m_s = +1$ level is energetically isolated and never populated by the driving field, we obtain:

$$d = d_c \frac{3\sin(2\alpha)\cos(\gamma)\sin(\theta')[\Delta - 3\gamma_e B_0 \cos(\theta')] - 6\gamma_e B_0 \sin^2(\alpha)\cos(2\gamma)\sin^2(\theta') + (3\cos(2\alpha)+1)(\Delta\cos(\theta') - \gamma_e B_0 \cos(2\theta'))}{4r^3\sqrt{2(\gamma_e B_0 \sin(\theta'))^2 + (\Delta - \gamma_e B_0 \cos(\theta'))^2}}$$

where $d_c = 2\pi \cdot 52.041$ kHz is the dipolar constant for two electronic spins at a distance of 1nm and $\theta' = \theta - \theta_{\mathrm{NV}}$ is the angle between the static magnetic field and the NV molecular axis in the $\mathbf{y}_{\mathrm{NV}} = 0$ plane.